



**HAL**  
open science

## Multiband corrections for the semi-classical simulation of interband tunneling in GaAs tunnel junctions

Kevin Louarn, Yann Claveau, Dimitri Hapiuk, Chantal Fontaine, Alexandre Arnoult, Thierry Taliercio, Christophe Licitra, François Piquemal, Alexandre Bounouh, Nicolas Cavassilas, et al.

► **To cite this version:**

Kevin Louarn, Yann Claveau, Dimitri Hapiuk, Chantal Fontaine, Alexandre Arnoult, et al.. Multiband corrections for the semi-classical simulation of interband tunneling in GaAs tunnel junctions. *Journal of Physics D: Applied Physics*, 2017, 50 (38), pp.385109. 10.1088/1361-6463/aa804e . hal-01610949

**HAL Id: hal-01610949**

**<https://laas.hal.science/hal-01610949>**

Submitted on 12 Jan 2023

**HAL** is a multi-disciplinary open access archive for the deposit and dissemination of scientific research documents, whether they are published or not. The documents may come from teaching and research institutions in France or abroad, or from public or private research centers.

L'archive ouverte pluridisciplinaire **HAL**, est destinée au dépôt et à la diffusion de documents scientifiques de niveau recherche, publiés ou non, émanant des établissements d'enseignement et de recherche français ou étrangers, des laboratoires publics ou privés.

**Multiband corrections for the semi-classical simulation of interband  
tunneling in GaAs tunnel junctions.**

K. Louarn<sup>1, 2</sup>, Y. Claveau<sup>3</sup>, D. Hapiuk<sup>4</sup>, C. Fontaine<sup>1</sup>, A. Arnoult<sup>1</sup>, T. Taliercio<sup>5</sup>,  
C. Licitra<sup>4</sup>, F. Piquemal<sup>2</sup>, A. Bounouh<sup>7</sup>, N. Cavassilas<sup>3</sup> and G. Almuneau<sup>1</sup>

<sup>1</sup> *LAAS-CNRS, Université de Toulouse, CNRS, Toulouse, France*

<sup>2</sup> *LNE, 29 avenue Roger Hennequin, F-78197, Trappes, France*

<sup>3</sup> *Aix Marseille Université, CNRS, Université de Toulon, IM2NP UMR 7334, 13397,  
Marseille, France*

<sup>4</sup> *Univ. Grenoble Alpes, F-38000 Grenoble, France*  
*CEA, LETI, MINATEC Campus, F-38054 Grenoble, France.*

<sup>5</sup> *Univ. Montpellier, IES, UMR 5214, F-34000, Montpellier, France*

<sup>6</sup> *CNRS, IES, UMR 5214, F-34000, Montpellier, France*

<sup>7</sup> *CEA LIST, Centre d'études, F-91400, Gif-sur-Yvette, France*

**Abstract:**

The aim of this study is to investigate the impact of multiband corrections on the current density of GaAs Tunnel Junctions (TJs) calculated with a refined yet simple Semi-Classical Interband Tunneling Model (SCITM). The non-parabolicity of the considered bands and the

spin-orbit effects are considered by using a recently revisited SCITM available in the literature. The model is confronted to experimental results from a series of Molecular Beam Epitaxy (MBE) grown GaAs TJs and to numerical results obtained with a full quantum model based on the Non-Equilibrium Green's Functions (NEGF) formalism and a 6-band k.p hamiltonian. We emphasize the importance of considering the non-parabolicity of the conduction band by two different measurements of the energy-dependent electron effective mass in N-doped GaAs. We also propose an innovative method to compute the non-uniform electric field in the TJ for the SCITM simulations, which is of prime importance for a successful operation of the model. We demonstrate that, when considering the multiband corrections and this new computation of the non-uniform electric field, the SCITM succeeds in predicting the electrical characteristics of GaAs TJs, and are also in agreement with the quantum model. Beside the fundamental study of the tunneling phenomenon in TJs, the main benefit of this SCITM is it can be easily embedded into drift-diffusion softwares, which are the most widely-used simulation tools for electronic and opto-electronic devices such as Multi-Junction Solar Cells (MJSCs), Tunnel Field-Effect Transistors (TFETs) or Vertical Cavity Surface Emitting Lasers (VCSELs).

## I-Introduction

Tunnel Junctions (TJs) are of prime importance for Multi-Junction Solar Cells (MJSCs), in which they ensure the series interconnection between each subcells. They consist in a P<sup>++</sup>/N<sup>++</sup> junction made of degenerately doped materials, which lead to a “broken-gap” like band diagram, as presented in Fig. 1. Consequently, electrons can tunnel from states located in one band to states located in the other band in a mechanism known as “interband tunneling”, as represented by the shaded area on Fig. 1. For MJSCs application, the TJ must operate in the low resistive interband tunneling region of its J-V characteristic which typically takes place in the [0-0.3V] voltage range, meaning that the photocurrent of the MJSC should never exceed the peak tunneling current density  $J_{\text{peak}}$ . Thus, the development of simulation tools able to accurately model the tunneling mechanism and quantify the J-V characteristic of TJs in this voltage range while being easy to implement in classic drift-diffusion software are of prime interest for photovoltaics applications, but also for other electronic and photonic devices integrating TJs such as VCSELs.

However, as pointed out in [1], the physical nature of the transport mechanisms in TJs has been a subject of debate in the literature, mainly because some of the widely-used interband tunneling models require an arbitrary adjustment of the fundamental materials parameters such as the effective masses [2] to successfully quantify the current density magnitude of TJs devices. Such calibration requirement has led to the hypothesis that other tunneling processes such as Trap-Assisted-Tunneling (TAT) could be the predominant mechanism in such devices, as presented in [3] or [4]. TAT models have thus been developed but have remained more or less empirical because of the complexity to collect accurate data on trap parameters in such highly-doped materials.

In a previous work [5], we presented a semi-classical interband tunneling model (SCITM) able to quantify the order of magnitude of GaAs TJs J-V characteristics while using established material parameters. To do so, the complex band structure of GaAs was considered to follow the 2-band Flietner's formula [6] but the real band structure of GaAs was nevertheless assumed to follow a parabolic approximation. As a result, it appeared that the predominant tunneling process in GaAs TJs is the direct  $\Gamma$ -valley Conduction Band (CB) / Light Hole Valence Band (LH-VB) interband transition rather than TAT related mechanisms. However, A. Pan and C. Chui have recently shown that the reliability of analytical SCITM can be improved when multiband corrections such as transverse non-parabolicity and spin-orbit coupling are considered [7]. Indeed, their corrected SCITM demonstrated a good theoretical agreement with Non-Equilibrium Green's Functions (NEGFs) based simulation of interband tunneling in InSb,  $\text{In}_{0.53}\text{Ga}_{0.47}\text{As}$  and InAs reversely biased p-n junctions.

In this work, we compare this refined yet simple SCITM with experimental J-V characteristics of GaAs TJs and with a Non-Equilibrium Green's Functions (NEGF) treatment of interband tunneling coupled with a 6-band k.p hamiltonian. A set of three MBE-grown GaAs TJs with various  $N_{++}$  doping levels, and thus with peak tunneling current densities  $J_{\text{peak}}$  in the range of 2 mA/cm<sup>2</sup> to 10 A/cm<sup>2</sup>, are used as experimental data as presented in Sec. II. The relevance of the considered band-structure of GaAs for the corresponding range of N doping levels is also highlighted in this section by experimental measurements of the energy dependent electron effective mass. In Sec. III, we remind the theories of the NEGF based simulations and the corrected SCITM. We propose in this section an innovative way to compute the non-uniform electrical field in the TJs that appears to be of great importance to successfully quantify the J-V characteristic of GaAs TJs as it is shown in Sec. IV. The influences of the multiband corrections and the Band-Gap-Narrowing (BGN) effect are also presented in Sec. IV.

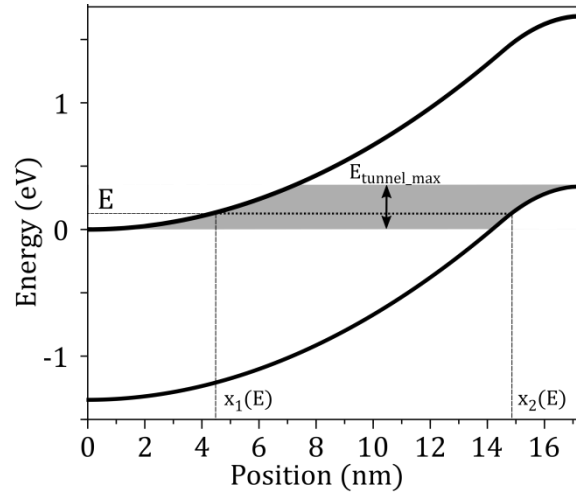


Fig. 1: Band diagram of GaAs TJ C (described in part II-1) at thermal equilibrium. The potential profile is calculated using the procedure of Sec. III-1, whereas the semi-classical “tunneling path” of an electron of energy  $E$  between its classical turning points  $x_1(E)$  and  $x_2(E)$  is represented by the dashed line in the band-gap. The energy range  $[0, E_{\text{tunnel\_max}}]$  for tunneling is represented by the shaded area.

## II-Experimental procedure and results

### 1-MBE growth and fabrication of GaAs TJs

Three GaAs TJs structures were fabricated on (001) N-GaAs substrate in a RIBER 32 MBE growth chamber using Si as a N-dopant and Be as a P-dopant. The samples are referred as TJ A, B and C, and were grown at a temperature of 580°C. As presented in Fig. 2, they consist in a P-degenerated layer of thickness 30 nm and  $N_a$  doping levels of  $3 \times 10^{19} \text{ cm}^{-3}$  (TJ A) or  $5 \times 10^{19} \text{ cm}^{-3}$  (TJ B and C), and a N-degenerated layer of thickness 30 nm with doping levels  $N_d$  of  $4.5 \times 10^{18} \text{ cm}^{-3}$  for TJ A,  $5.8 \times 10^{18} \text{ cm}^{-3}$  for TJ B and  $[9-9.5] \times 10^{18} \text{ cm}^{-3}$  for TJ C. These doping levels were previously calibrated by Hall measurements on specifically designed samples. However, because of well-known compensation issues in heavily Si doped GaAs [8], we performed also post-growth measurement of the Si concentrations in TJ C by Secondary Ions Mass Spectroscopy (SIMS). The Si content measured by SIMS in TJ C is of  $1.3 \times 10^{19} \text{ cm}^{-3}$ , which indeed corresponds to a  $N_{++}$  doping level close to  $9.5 \times 10^{18} \text{ cm}^{-3}$  according to the results of [8] for homogeneously Si doped GaAs layers grown at 580°C. The doping levels for TJ A, B and C are reminded in the table II of Sec. IV.

These two degenerated layers are surrounded by  $2 \times 10^{18} \text{ cm}^{-3}$  N-doped and P-doped 300 nm thick buffer layers. A  $1 \times 10^{19} \text{ cm}^{-3}$  P-doped 50 nm thick cap layer is grown on top of the structure to ensure a good ohmic contact. Mesa-isolated circular diodes of diameter in the range of [200  $\mu\text{m}$  – 800  $\mu\text{m}$ ] were fabricated by photolithography and chemical etching, followed by a Ti/Au (50 nm / 200 nm) metal deposition on top of the mesas and on the back side of the substrate. The J-V characteristics of the TJs were measured using a Karl Suss PA200 probe station at room temperature. TJ A reached a relatively low  $J_{\text{peak}}$  of 2 mA/cm<sup>2</sup>, whereas TJ B reached  $J_{\text{peak}}=65 \text{ mA/cm}^2$  and TJ C reached  $J_{\text{peak}}=10 \text{ A/cm}^2$ . The corresponding J-V characteristics are presented in Fig. 5-a), -b) and -c).

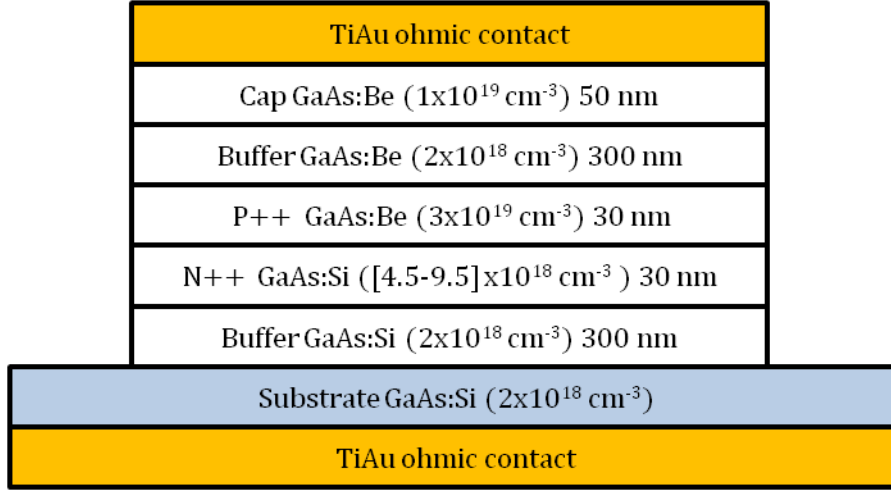


Fig. 2: Final MBE grown GaAs TJs structure, with metal deposition on the top and the bottom of the mesa-isolated diode.

## 2- Experimental measurement of electrons effective mass dependence with carrier's energy

As described in Sec. III-2, the GaAs band structure is considered to follow a 4-band k.p model, and the CB non-parabolicity can be expressed into energy-dependent effective mass according to formula (14). We experimentally verified the energy-dependence of the electron effective mass  $m_e^*(E)$  on N-doped GaAs samples by tracking the corresponding plasmon frequency  $\omega_p$  of the “Brewster mode” either by InfraRed Spectroscopic Ellipsometry (IRSE) measurements [9] or infrared reflectometry measurements [10]. Unfortunately, the same measurements methods cannot be directly applied for the energy-dependence of the LH effective mass  $m_{lh}^*(E)$ . Indeed, the measurements of  $m_{lh}^*(E)$  is complicated by the presence of the Heavy Hole valence band, as only 7% of holes are located in the LH-VB [11].

We performed both ellipsometry and reflectometry measurements at room-temperature of the energy-dependence of the electron effective mass (using a Woollam IR-VASE spectroscopic ellipsometer and the modified Fourier Transform InfraRed (FTIR) system

described in [10]). Measurements were done on a series of seven N doped Hall calibrated samples (referenced as Hall 1 to 7) consisting in a layer of 1  $\mu\text{m}$  thick GaAs:Si grown on a semi-insulating (001) GaAs substrate. Samples Hall 1 to Hall 4 were measured by reflectometry whereas additional ellipsometry measurements of samples Hall 5 to Hall 7 were performed to ensure the convergence of both measurements methods. From the doping levels, one can calculate the Fermi Level position in the CB as presented in part III-1 and thus determine the value of the electron effective mass as function of the carrier energy inside the CB using formula (1):

$$m_e^*(E) = \frac{N_d q^2}{\epsilon_\infty \omega_p^2} \quad (1)$$

In formula (1),  $\epsilon_\infty$  correspond to the high-frequency electric constant, equal to 10.89 (in units of  $\epsilon_0$ , at 300K) in GaAs, whereas  $q$  is the electron elementary charge. The doping levels and the corresponding Fermi-Level energies of samples Hall 1 to Hall 7 are reported in the table I below.

Parameters	Values						
	Hall 1	Hall 2	Hall 3	Hall 4	Hall 5	Hall 6	Hall 7
<b><math>N_D</math> (<math>10^{18} \text{ cm}^{-3}</math>)</b>	1.75	2.6	4.8	6.1	0.1	1	5.1
<b>Relative Fermi Energy (eV)</b>	0.07	0.097	0.147	0.168	-0.036	0.043	0.154

Table I. Hall Effect measurements of the doping level and corresponding Fermi energy level of n-doped GaAs Samples labelled Hall 1 to 7

The reflectometry measurements of the electron effective mass as function of the doping levels of the samples 1 to 4 are represented by the red dots on the graph of Fig. 3, whereas the ellipsometry measurements for samples 5 to 7 are represented by the blue dots. The black curve corresponds to the theoretical variation of the electron effective mass as function of the carrier density, as presented in part III-3-b. As shown on Fig. 3, there is overall a good agreement between the two measurements and the theoretical curve. Both experimental measurement methods show that there is a significant variation of the electron effective mass value for Fermi energy above 40 meV, which corresponds to doping levels exceeding  $10^{18} \text{ cm}^{-3}$ . The good agreement between the theory and the experimental measurements highlights the relevance of using the 4-band k.p theory for considering the non-parabolicity of the considered bands, at least for the CB in this range of doping levels.

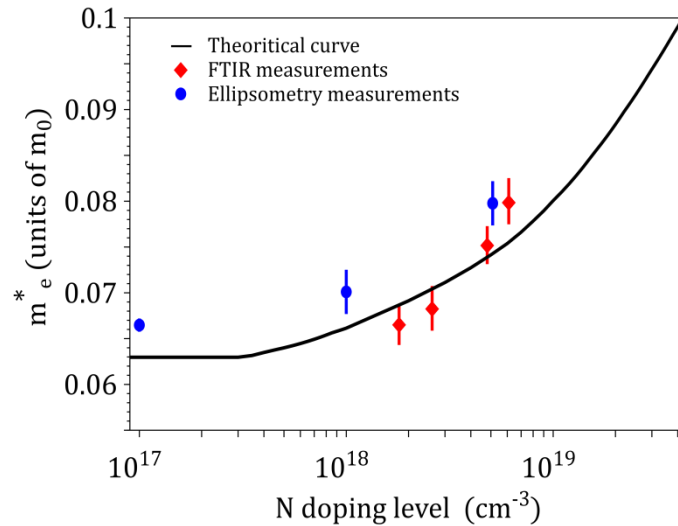


Fig. (3). Experimental (blue points and red points for ellipsometric and FTIR measurements respectively) and theoretical (black curve) variations of the GaAs electrons effective mass as a function of the doping levels in the different samples.

### III- Description of the models

In this part, we summarize the theory of the two models used for the simulation of the tunneling carriers' transport in the GaAs TJs. The Kane tunneling formulae that enable to compute the tunneling current density in an embeddable way for the SCITM model as well as the multiband corrections of [7] are reminded. Our procedure to evaluate of the non-uniform electric field in the TJ is also presented. On the other hand, the more elaborated full quantum model based on NEGF formalism allows to compute the tunneling current density without parameter adjustment (other than the band parameters of the k.p hamiltonian), and thus is considered as a reference model to validate the accuracy of the SCITM. In order to ensure a good comparison between the two numerical results, the same potentials are used for both models. Because we are only considering the direct  $\Gamma$ -valley CB/VB interband tunneling transition in the [001] direction, the tunneling process is unidimensional along the corresponding x-axis and the transverse momentum must be conserved.

#### 1-Potential evaluation of the GaAs TJs with band gap narrowing.

As already described in [5], we model the TJ band diagram as an abrupt P+/N+ GaAs junction. The reference energy and position are chosen to be at the band edge of the CB's n-side, meaning that  $E_{C(x=0)}=0$  eV. Because of the degenerate nature of the TJ's materials, the relative position of the Fermi levels  $F_n$  and  $F_p$  for the n-side and p-side of the TJ at thermal equilibrium are evaluated using either the Joyce-Dixon approximation [12] or the semi-metallic approximation according to formula (2), depending on the value of the ratio  $\frac{N_a}{N_v}$  and  $\frac{N_d}{N_c}$  where  $N_v$  and  $N_c$  are the VB and CB effective density of states respectively. Note that for high Fermi energy, one must include the energy dependence of the CB effective density of states due to the non-parabolicity of the band [13]. For the VB effective density of states, the impact

of the non-parabolicity of the LH-VB can be neglected as it represents only 7% of the total number of holes in the VB.

$$\left[ \begin{array}{l} \frac{F_n(\text{resp. } p)}{k_B T} \approx \ln \left( \frac{N_d(\text{resp. } a)}{N_c(\text{resp. } v)} \right) + \frac{1}{\sqrt{8}} \frac{N_d(\text{resp. } a)}{N_c(\text{resp. } v)} \\ \quad - \left( \frac{3}{16} - \frac{\sqrt{3}}{9} \right) \left( \frac{N_d(\text{resp. } a)}{N_c(\text{resp. } v)} \right)^2 + \dots, \quad 0.144 \leq \frac{N_d(\text{resp. } a)}{N_c(\text{resp. } v)} < 4.19 \\ \frac{F_n(\text{resp. } p)}{k_B T} \approx \left( \frac{3\sqrt{\pi}}{4} \frac{N_d(\text{resp. } a)}{N_c(\text{resp. } v)} \right)^{\frac{2}{3}}, \quad \frac{N_d(\text{resp. } a)}{N_c(\text{resp. } v)} \geq 4.19 \end{array} \right. \quad (2)$$

In equations (2),  $k_B$  is the Boltzmann constant and  $T$  is the temperature. From the relative position of the Fermi levels, the built-in voltage  $V_{bi}$ , the depletion length  $W_n$  and  $W_p$  in the n-side and p-side respectively and the TJ's band diagram are evaluated using Shockley formulae (3).

$$\left\{ \begin{array}{l} E_c(x) = q \frac{N_d x^2}{2 \varepsilon}, \quad x \leq W_n \text{ with } W_n = W \frac{N_a}{N_a + N_d} \\ E_c(x) = (V_{bi} - V_{app}) - q \frac{N_a (W-x)^2}{2 \varepsilon}, \quad x \geq W_n \\ E_v(x) = E_c(x) - E_g \end{array} \right. \quad (3)$$

In formulae (3),  $E_c(x)$ ,  $E_v(x)$  and  $E_g$  are the CB and VB edge spatial profile and the band-gap energy respectively.

As mentioned in [14], the BGN is an important effect related to degenerated semiconductors that had to be considered in GaAs TJs numerical simulation. Although the well-known Jain-Roulston BGN model gives a quite valuable evaluation of the BGN in N-type GaAs [15] and P-type GaAs [16] at low temperature, there is not, to the best of our knowledge, any accurate GaAs BGN model at room temperature. Moreover, accurate BGN corrections considerably complicate the potential evaluation because the TJs have to be

modeled as a tunnel heterojunction with the corresponding CB and VB offsets, as presented in the work of [17].

Fortunately, simulations with the NEGF model combined with an accurate knowledge of the experimental doping levels of TJ A, B and C allows to treat the global BGN in the whole TJ structure as an adjustment variable, as it is the only unknown parameter. Thus, this simulation procedure permits to only focus on the impact of the multiband corrections in the SCITM with an elementary treatment of the BGN, thus offsetting the lack of accurate and simple evaluation of this effect. The BGN values for TJ A, B and C, as well as the Fermi levels  $F_n$  and  $F_p$  at thermal equilibrium, the CB and VB effective density of states and others relevant potential related parameters are summarized in table II of Sec. IV.

## 2- NEGF based quantum model

Amongst many advantages, the use of Keldysh's perturbation theory for non-equilibrium system allows to take into account many body effects as well as quantum behaviors. In particular, tunneling current can be directly obtained without the requirements of any adjustment parameters, nor transfer hamiltonian, as shown in the seminal paper of [18]. Following the latter, we have used a 6-band k.p hamiltonian explicitly taking into account all the interband couplings between the heavy-hole band, the light-hole band and the first direct conduction band. All parameters are given in [19]. Within this framework, we assume a one-dimensional description of the TJ (the system is invariant in the transverse plane, see [20] for more details) and only ballistic current as it appears that scattering does not change much the current (not shown here). The complete description of the model should be published elsewhere soon. Moreover, in order to make a proper comparison between this quantum approach and the semi-classical one, we have used the same empirical potential in both approaches (see Fig. 1).

### 3- SCITM with 2-band approximation and multiband corrections

#### a- SCITM with 2-band approximation

The tunneling current density in a bulk TJ is expressed according well-known formula (3) [21].

$$J = \frac{q}{\pi\hbar} \int \frac{dk_{\perp}^2}{(2\pi)^2} \int_{-\infty}^{+\infty} dE T(E, k_{\perp}) [f_c(E) - f_v(E)] \quad (4)$$

In formula (3),  $\hbar$  is the reduced Planck's constant,  $k_{\perp}$  is the transverse momentum perpendicular to the tunneling direction,  $T(E, k_{\perp})$  is the tunneling probability of the electrons of total energy  $E$  and perpendicular momentum  $k_{\perp}$ , whereas  $f_c(E)$  and  $f_v(E)$  are the Fermi distribution in the CB and VB on each corresponding sides of the TJ.

In the semi-classical scheme, the tunneling probability can be computed numerically using the Wetzmer-Kramer-Brillouin (WKB) approximation. For a tunneling electron of energy  $E$  and no perpendicular momentum, the WKB tunneling probability is evaluated from the semi-classical formulation of the imaginary wavevector  $k_x$  between the classical turning points  $x_1$  and  $x_2$  as illustrated in Fig.1. The corresponding formulation of the tunneling probability is given in formula (5)

$$T_{WKB}(E, k_{\perp} = 0) = \exp\left(-2 \int_{x_1}^{x_2} k_x(E, k_{\perp} = 0) dx\right) \quad (5)$$

As we recommended in [5], the imaginary wave vector  $k_x$  of the tunneling carrier inside the band-gap can be evaluated using the 2-band Flietner's relation (6), that is well-adapted to model the complex band structure of material whose bands effective masses values differs as in GaAs [22]:

$$k_{x,Flieetner}(E, k_{\perp} = 0) = \frac{\sqrt{2m_0}}{i\hbar} \sqrt{\frac{E_g(E_c(x)-E)(E_v(x)-E)}{\left(\sqrt{\frac{1}{m_{e0}^*}}(E_v(x)-E) - \sqrt{\frac{1}{m_{lh0}^*}}(E_c(x)-E)\right)^2}} \quad (6)$$

The effect of the transverse momentum on the tunneling current density can be considered by the corresponding modified band gap  $Eg(k_{\perp})$ , as presented in [23]. In the Kane's formulation of interband tunneling [24], the effect of the transverse momentum is rather considered by integrating analytically the tunneling probability under the assumption of a constant electric field  $F$ , but we still use formula (5) to derive an accurate value of  $F$  as presented in Sec. III-3-c. Under the assumption of a constant electric field  $F$ , the tunneling probability is given by:

$$T_{Kane}(E, k_{\perp}) = \frac{\pi^2}{9} \exp\left(-\frac{B_{Kane}}{F}\right) \exp\left(-2\frac{E_{\perp}}{\bar{E}_{\perp Kane}}\right) \quad (7)$$

In formula (7),  $E_{\perp}$  is the transverse energy associated with the transverse momentum  $k_{\perp}$ , whereas the value of  $B_{Kane}$  and  $\bar{E}_{\perp Kane}$  are given by formulae (8-a) and 8-b) when a 2-band relation is considered. The constant electric field assumption thus makes it possible to directly consider the effect of the perpendicular momentum in the tunneling probability.

$$B_{Kane} = \frac{\pi m_r^{\frac{1}{2}} E_g^{\frac{3}{2}}}{2q\hbar} \quad (8-a)$$

$$\bar{E}_{\perp Kane} = \frac{2q\hbar F}{\pi m_r^{\frac{1}{2}} E_g^{\frac{1}{2}}} \quad (8-b)$$

The reduced effective mass  $m_r$  is evaluated from CB and LH-VB band-edge effective mass  $m_{e0}$  and  $m_{lh0}$  :

$$m_r = \frac{m_{e0} m_{lh0}}{m_{e0} + m_{lh0}} \quad (9)$$

When a parabolic approximation is considered for the bands, the integration of formula (4) over  $k_{\perp}$  gives immediately the tunneling current density:

$$J_{Kane} = \int_0^{E_{tunnel-max}} dE A_{Kane}(F) \exp\left(-\frac{B_{Kane}}{F}\right) [f_c(E) - f_v(E)] \quad (10)$$

In formula (10),  $E_{tunnel-max}$  is the maximum energy for tunneling, as presented on Fig. (1), and the field-dependent prefactor  $A_{Kane}(F)$  is given by:

$$A_{Kane}(F) = \frac{q^2 BF}{9\pi^2 \hbar E_g^2} \quad (11)$$

### b- SCITM with multiband corrections

In [7], a 8-band k.p hamiltonian is used to model the GaAs band structure with eigenvalues given by formulae (12), that are equivalent to the Kane's 4-band k.p model [25]:

$$\begin{cases} E' = 0 \\ E'(E' - E_g)(E' + \Delta) - k^2 P^2 \left(E' + \frac{2\Delta}{3}\right) = 0 \end{cases} \quad (12)$$

In formulae (12),  $E' = E - \frac{\hbar^2 k^2}{2m_0}$ ,  $P$  is the momentum matrix element that can be evaluated from the Kane energy  $E_p = \frac{2m_0 P^2}{\hbar^2}$  and  $\Delta$  is the split-off energy.

Following the procedure of [13], the CB dispersion relation can be expressed as:

$$\begin{cases} E \approx \frac{\hbar^2 k^2}{2m_{e0}^*} + \frac{\alpha}{E_g} \left(\frac{\hbar^2 k^2}{2m_{e0}^*}\right)^2 \\ \alpha = -\frac{(1 - m_{e0}^*)^2 (3E_g^2 + 4E_g \Delta + 2\Delta^2)}{(E_g + \Delta)(3E_g + 2\Delta)} \end{cases} \quad (13)$$

The values of  $E_p$ ,  $\Delta$  and  $\alpha$  are reported in Table II.

The electron energy-dependant effective mass is thus defined by:

$$m_e^*(E) = m_{e0}^* \left( 1 - 2\alpha \frac{E}{E_g} \right) \quad (14)$$

The theoretical curve of  $m_e^*(E)$  is presented in Fig. 3, and shows a reasonable agreement with the ellipsometry and reflectometry measurements, thus confirming the appropriateness of using formulae (12) to model the GaAs band structure in our range of doping levels.

From formulae (12), the 4-band imaginary wave vector expression is given by:

$$k_{x,4 \text{ band}}(E, k_{\perp}) = \frac{1}{iP} \sqrt{\frac{(E_c(x)-E)(E_v(x)-E)(Ec(x)-E+\Delta)}{(Ec(x)-E+\frac{2\Delta}{3})}} \quad (15)$$

The multiband corrections obtained with formulae (12) and (15) under a constant field-assumption give modified non-parabolic parameters  $B_{NP}$  and  $A_{NP}(F)$  to evaluate the tunneling current density:

$$B_{NP} = \frac{\pi m_r^2 E_g^2}{2q\hbar} \sqrt{\frac{(5+4 \Delta/E_g) (1+2 \Delta/E_g)}{(2+2 \Delta/E_g) (3+4 \Delta/E_g)}} \quad (16)$$

$$A_{NP}(F) = \frac{q^2 B_{NP} F}{9\pi^2 \hbar E_g^2} + \frac{q^3 F^2}{18\pi^2 \hbar E_g^2} \quad (17)$$

$$J_{NP} = \int_0^{E_{tunnel-max}} dE A_{NP}(F) \exp\left(-\frac{B_{NP}}{F}\right) [f_c(E) - f_v(E)] \quad (18)$$

### c- Non-uniform electric field evaluation

Numerical integration of WKB tunneling probability for each given energy E enable to take into account the real spatial profile of the CB and VB in the calculation; the spatial variation of the electric field is thus considered. However, the integration over  $k_{\perp}$  in formula

(4) is greatly simplified under a constant electric-field assumption, to the cost of a loss of accuracy as the spatial variation of the electric field is important in TJs.

The use of an energy-dependent electric field  $F(E)$  and a numerical integration of formulae (10) and (18) enable to partially solve this issue. In [7], the use of the average field  $F_{ave}(E) = \frac{Eg}{w}$  with  $w=x_2-x_1$  is recommended. We rather propose to compute the energy-dependent electric field  $F_{eq.}(E)$  from equivalence between the WKB tunneling probability computed numerically and the analytical one for tunneling electrons of energy  $E$  with no transverse momentum, as presented in formulae (19) and (20):

$$\left\{ \begin{array}{l} T_{WKB \text{ Flietner (resp. 4band)}}(E, k_{\perp} = 0) = T_{Kane \text{ (resp. NP)}}(F(E), k_{\perp} = 0) \quad (19) \\ \Leftrightarrow F_{Kane \text{ (resp. NP) eq.}}(E) = -\frac{B_{Kane \text{ (resp NP)}}}{\ln\left(\frac{9}{\pi} T_{WKB \text{ Flietner (resp. 4band)}}(E, k_{\perp}=0)\right)} \quad (20) \end{array} \right.$$

Using this procedure to consider the non-uniformity of the electric field, we ensure that the real spatial profile of the CB and VB are taken into account in the tunneling probability evaluation, whereas the simplicity of formulae (10) and (18) is preserved. We will see in the following Sec. IV that this procedure to evaluate the electric field should be used for quantifying the tunneling current density of GaAs TJs.

## IV-Results and discussion

### 1- NEGF quantum model, multiband SCITM and 2-band SCITM results

The experimental (black cross) and simulated J-V characteristics of TJ A, B and C using the SCITM with the 2-band approximation (long dashed-green curve), the SCITM with the multiband corrections (short dashed-blue curve) and the full quantum model (solid red curve) are presented in Fig. 4. The corresponding relevant experimental and simulation parameters are given in the Table II, whereas the values of the peak tunneling current densities are reported in Table III. For the SCITM simulations of Fig. 4, we use the non-uniform electric field computed with the procedure detailed in Sec. III-3-c). The recommended value of  $E_P$  for a 4-band k.p model of GaAs is  $E_P \approx 22.7$  eV [26] and its range of validity is [20-25 eV]. Because of the BGN effect,  $E_P$  has to be reduced for TJ B and C and the corresponding values are reported in Table II. A non-empirical dependence of  $E_P$  with the BGN is under investigation.

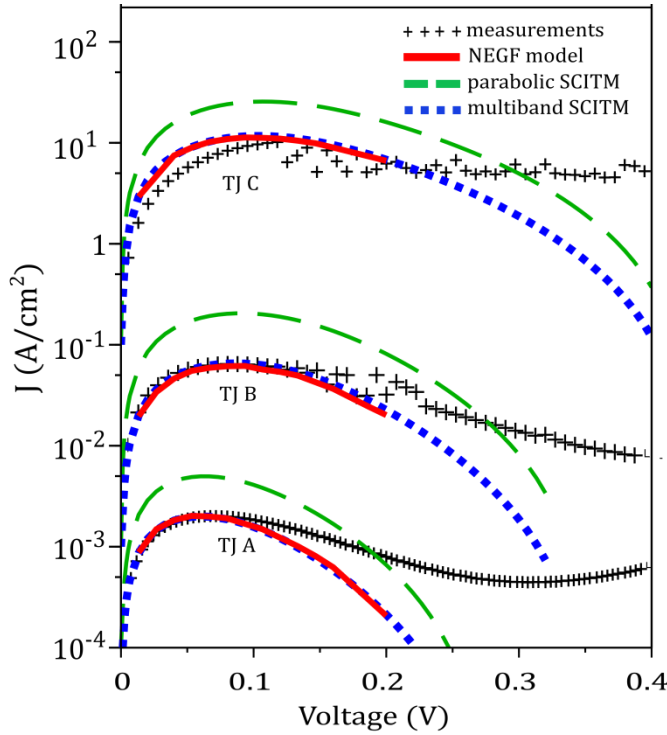


Fig. 4- Experimental, semi-

classical and NEGF simulated J-V characteristics of TJ A, B and C.

Parameters		Value		
		TJ A	TJ B	TJ C
E <sub>g</sub> (eV)	Without BGN	1.424		
	With BGN	1.424	1.41	1.373
N <sub>d</sub> (cm <sup>-3</sup> )		4.5x10 <sup>18</sup>	5.8x10 <sup>18</sup>	9.5x10 <sup>18</sup>
N <sub>a</sub> (cm <sup>-3</sup> )		3x10 <sup>19</sup>	5x10 <sup>19</sup>	5x10 <sup>19</sup>
N <sub>c</sub> (cm <sup>-3</sup> )		4.22x10 <sup>17</sup>	4.35x10 <sup>17</sup>	4.85x10 <sup>17</sup>
N <sub>v</sub> (cm <sup>-3</sup> )		9.5x10 <sup>18</sup>		
F <sub>n</sub> (eV)		0.14	0.16	0.22
F <sub>p</sub> (eV)		0.0678	0.0945	0.0945
V <sub>bi</sub> (V)		1.63	1.67	1.69
m <sub>e0</sub> <sup>*</sup> (units of m <sub>0</sub> )		0.063		
m <sub>lh0</sub> <sup>*</sup> (units of m <sub>0</sub> )		0.082		
α		-0.83		
E <sub>p</sub> (eV)		21.4	20.5	20

Table II. Experimental and simulation parameters used for the evaluation of the potentials and the tunneling current densities of TJ A, B and C.

The NEGF based quantum model as well as the SCITM with the multiband corrections succeed to quantify the magnitude of the tunneling current density for all of the

TJs. On contrary, the 2-band SCITM without corrections largely overestimates the tunneling current density magnitude. Such results demonstrate the important of the multiband corrections in the SCITM. However, the BGN consideration and mostly the evaluation of the non-uniform electric field are also very important to quantify the tunneling current density of GaAs TJs, as it is presented in the two following sections.

Due to their relatively low intrinsic resistance, the J-V curves of TJs B and C exhibit classical measurement instabilities in their Negative Differential Resistance (NDR) region II. The small discrepancies between the experimental curve and the theoretical ones in the valley region and in the slope of the J-V curve are due to trap-related excess current [1] and to parasitic series resistance effects [27]. As we focus only on the magnitude of the tunneling current, we did not take into account these two well-known effects in the presented numerical results.

## **2- Influence of the Band-Gap Narrowing**

As mentioned in Sec. III-1, a global BGN is empirically considered for each TJ with the help of the quantum model. This correction is of prime importance to successfully quantify the tunneling current density for highly doped TJs. Indeed, whereas the BGN is found to be negligible for the relatively “low” doped TJ A, significant values of 1.41 eV and 1.373 eV have been found for TJ B and C respectively. Without the BGN consideration, the peak tunneling current densities  $J_{\text{peak}}$  of TJ C evaluated with the quantum model and the SCITM with the multiband corrections are only of 6 A/cm<sup>2</sup>, which represent a discrepancy up to 40 % with the experimental results. A non-empirical description of the BGN effect in TJ is under investigation, but is seriously complicated by the lack of accurate models able to quantify it at room temperature.

## **3- Importance of the non-uniform electric field evaluation**

The evaluation of the electric field is a key step in Kane’s derivation of the interband tunneling current density (and by extension for the multiband corrected SCITM). The overall good agreement of the two SCITMs with the NEGF model and the experimental measurements is in fact mainly due to our procedure to evaluate the non-uniform electric field described in Sec. III-3-c. Indeed, if we use the average electric field as proposed in [7] – which was shown to be still superior to other electric field computations – the current densities of the TJs are seriously underestimated as presented in Table III below.

		$J_{\text{peak}}$ (A/cm <sup>2</sup> )		
		TJ A	TJ B	TJ C
Experimental measurements		$2 \times 10^{-3}$	$6.5 \times 10^{-2}$	10
NEGF based model		$2 \times 10^{-3}$	$6.4 \times 10^{-2}$	11
2-band SCITM	$F_{\text{Kane eq.}}$	$5 \times 10^{-3}$	$2 \times 10^{-1}$	26
	$F_{\text{ave.}}$	$3.5 \times 10^{-4}$	$1 \times 10^{-2}$	3.5
multiband SCITM	$F_{\text{NP eq.}}$	$2 \times 10^{-3}$	$6.5 \times 10^{-2}$	10.5
	$F_{\text{ave.}}$	$2.2 \times 10^{-4}$	$2.2 \times 10^{-3}$	2

Table III. Measured and computed  $J_{\text{peak}}$  value for TJs A, B and C. The NEGF model and the SCITM integrating the multiband corrections as well as the non-uniformity of the electric field as presented in Sec III-c predict  $J_{\text{peak}}$  values very close to the experimental one.

For the reasons already explained in Sec. III-3-c, our procedure to evaluate the electric field for each “tunneling path” in the TJ enables to take advantage of the ability of a numerical integration of the WKB tunneling probability to describe the real potential profile while keeping the simplicity of Kane’s formulation to consider the effect of transverse

momentum. Thus, the global accuracy of the SCITM is improved with minimal computational efforts.

## **V-Conclusion**

We have used a NEGF / 6-band  $k,p$  based model, a 2-band based SCITM and a multiband SCITM to model the experimental J-V characteristics of GaAs TJs which extend on a wide range of performances. The accurate – but more complicated – NEGF model has shown that the BGN consideration is of main importance for heavily doped TJs, and of course succeeds to predict the current density of the experimental devices. We have also shown that the multiband corrections as well as an appropriate evaluation of the non-uniformity of the electric field in the TJs enable to get accurate results with simple semi-analytical SCITM. We thus propose an innovative way to compute the non-uniform electric field from equivalence between numerical integration of the WKB tunneling probability and the analytical Kane's tunneling probability. Following the work of [22] and [28], this electric field evaluation procedure could be extended to more complicated structures such as tunnel heterojunctions and quantum confined systems. Such corrected SCITM represents a good compromise between accuracy and simplicity as it can be easily implemented into drift diffusion softwares, which are of main interest for the simulation of devices integrating TJs such as MJSCs or VCSEL.

## **Acknowledgements**

This work was supported financially by the EURAMET agency in the frame of JRP ENG51 SolCell project, and by the ANRT-CIFRE. The EMRP is jointly funded by the EMRP participating countries within EURAMET and the European Union. The financial support of the project ANR-14-CE26-0020-01 "Platofil" is also acknowledged. This work was partly supported by LAAS-CNRS micro and nanotechnologies platform, a member of the French

RENATECH network. The authors acknowledge Dr. Stéphane Calvez for scientific discussions and proofreading.

## Bibliography

- [1] A. W. Walker, O. Theriault, M. M. Wilkins, J. F. Wheeldon, and K. Hinzer, "Tunnel-junction-limited multijunction solar cell performance over concentration," *Sel. Top. Quantum Electron. IEEE J. Of*, vol. 19, no. 5, pp. 1–8, 2013.
- [2] M. Hermle, G. Létay, S. P. Philipps, and A. W. Bett, "Numerical simulation of tunnel diodes for multi-junction solar cells," *Prog. Photovolt. Res. Appl.*, vol. 16, no. 5, pp. 409–418, Aug. 2008.
- [3] M. Baudrit and C. Algora, "Tunnel diode modeling, including nonlocal trap-assisted tunneling: a focus on III–V multijunction solar cell simulation," *Electron Devices IEEE Trans. On*, vol. 57, no. 10, pp. 2564–2571, 2010.
- [4] K. Jandieri *et al.*, "Resonant electron tunneling through defects in GaAs tunnel diodes," *J. Appl. Phys.*, vol. 104, no. 9, p. 94506, 2008.
- [5] K. Louarn *et al.*, "Modelling of interband transitions in GaAs tunnel diode," *Semicond. Sci. Technol.*, vol. 31, no. 6, p. 06LT01, Jun. 2016.
- [6] H. Flietner, "The E (k) Relation for a Two-Band Scheme of Semiconductors and the Application to the Metal-Semiconductor Contact," *Phys. Status Solidi B*, vol. 54, no. 1, pp. 201–208, 1972.
- [7] A. Pan and C. O. Chui, "Modeling direct interband tunneling. I. Bulk semiconductors," *J. Appl. Phys.*, vol. 116, no. 5, p. 54508, Aug. 2014.
- [8] K. Köhler, P. Ganser, and M. Maier, "Comparison of Si  $\delta$ -doping with homogeneous doping in GaAs," *J. Cryst. Growth*, vol. 127, no. 1–4, pp. 720–723, Feb. 1993.
- [9] G. Leibiger, V. Gottschalch, and M. Schubert, "Optical functions, phonon properties, and composition of InGaAsN single layers derived from far- and near-infrared spectroscopic ellipsometry," *J. Appl. Phys.*, vol. 90, no. 12, p. 5951, 2001.
- [10] T. Taliercio, V. N. Guilengui, L. Cerutti, E. Tournié, and J.-J. Greffet, "Brewster 'mode' in highly doped semiconductor layers: an all-optical technique to monitor doping concentration," *Opt. Express*, vol. 22, no. 20, p. 24294, Oct. 2014.
- [11] L. D. Zivanov and M. B. Zivanov, "Determination of average effective masses of majority carriers as function of impurity concentrations for heavily doped GaAs," in *Semiconductor Conference, 1995. CAS'95 Proceedings., 1995 International*, 1995, pp. 103–106.
- [12] W. B. Joyce and R. W. Dixon, "Analytic approximations for the Fermi energy of an ideal Fermi gas," *Appl. Phys. Lett.*, vol. 31, no. 5, p. 354, 1977.
- [13] J. S. Blakemore, "Semiconducting and other major properties of gallium arsenide," *J. Appl. Phys.*, vol. 53, no. 10, p. R123, 1982.
- [14] A. Lebib, R. Hannanchi, L. Beji, and B. EL Jani, "Effect of band gap narrowing on GaAs tunnel diode I-V characteristics," *Phys. B Condens. Matter*, vol. 502, pp. 93–96, Dec. 2016.
- [15] S. C. Jain, J. M. McGregor, D. J. Roulston, and P. Balk, "Modified simple expression for bandgap narrowing in n-type GaAs," *Solid-State Electron.*, vol. 35, no. 5, pp. 639–642, 1992.

- [16] S. C. Jain, J. M. McGregor, and D. J. Roulston, "Band-gap narrowing in novel III-V semiconductors," *J. Appl. Phys.*, vol. 68, no. 7, p. 3747, 1990.
- [17] W.-S. Cho *et al.*, "Full band atomistic modeling of homo-junction InGaAs band-to-band tunneling diodes including band gap narrowing," *Appl. Phys. Lett.*, vol. 100, no. 6, p. 63504, 2012.
- [18] C. Caroli, R. Combescot, P. Nozieres, and D. Saint-James, "Direct calculation of the tunneling current," *J. Phys. C Solid State Phys.*, vol. 4, no. 8, pp. 916–929, Jun. 1971.
- [19] I. Vurgaftman, J. R. Meyer, and L. R. Ram-Mohan, "Band parameters for III–V compound semiconductors and their alloys," *J. Appl. Phys.*, vol. 89, no. 11, p. 5815, 2001.
- [20] N. Cavassilas, F. Michelini, and M. Bescond, "Modeling of nanoscale solar cells: The Green's function formalism," *J. Renew. Sustain. Energy*, vol. 6, no. 1, p. 11203, Jan. 2014.
- [21] D. J. BenDaniel and C. B. Duke, "Space-charge effects on electron tunneling," *Phys. Rev.*, vol. 152, no. 2, p. 683, 1966.
- [22] D. Sarkar, M. Krall, and K. Banerjee, "Electron-hole duality during band-to-band tunneling process in graphene-nanoribbon tunnel-field-effect-transistors," *Appl. Phys. Lett.*, vol. 97, no. 26, p. 263109, 2010.
- [23] W. Vandenberghe, B. Sorée, W. Magnus, and G. Groeseneken, "Zener tunneling in semiconductors under nonuniform electric fields," *J. Appl. Phys.*, vol. 107, no. 5, p. 54520, Mar. 2010.
- [24] E. O. Kane, "Theory of Tunneling," *J. Appl. Phys.*, vol. 32, no. 1, p. 83, 1961.
- [25] E. O. Kane, "Band structure of indium antimonide," *J. Phys. Chem. Solids*, vol. 1, no. 4, pp. 249–261, Jan. 1957.
- [26] G. Bastard and J. Schulman, *Wave mechanics applied to semiconductor heterostructures*. 1992.
- [27] J. F. Wheeldon *et al.*, "Performance comparison of AlGaAs, GaAs and InGaP tunnel junctions for concentrated multijunction solar cells," *Prog. Photovolt. Res. Appl.*, vol. 19, no. 4, pp. 442–452, Jun. 2011.
- [28] A. Pan and C. O. Chui, "Modeling direct interband tunneling. II. Lower-dimensional structures," *J. Appl. Phys.*, vol. 116, no. 5, p. 54509, Aug. 2014.